Journal of Materials Chemistry A

PAPER

View Article Online
View Journal | View Issue

Cite this: J. Mater. Chem. A, 2017, 5, 4991

Influence of ionic conductivity of the nano-particulate coating phase on oxygen surface exchange of $La_{0.58}Sr_{0.4}Co_{0.2}Fe_{0.8}O_{3-\delta}$

Saim Saher,†[a] Sahir Naqash,‡[a] Bernard A. Boukamp,[a] Bobing Hu,[b] Changrong Xia[b] and Henny J. M. Bouwmeester*[ab]

Received 20th December 2016
Accepted 5th February 2017

DOI: 10.1039/c6ta10954c

rsc.li/materials-a

The oxygen surface exchange kinetics of mixed-conducting perovskite $La_{0.58}Sr_{0.4}Co_{0.2}Fe_{0.8}O_{3-\delta}$ (LSCF) ceramics coated with a porous nano-particulate layer of either gadolinea (Gd_2O_3), ceria (CeO_2) or 20 mol% Gd-doped ceria (GCO) was determined by electrical conductivity relaxation (ECR). The measurements were performed in the temperature range 700–900 °C, following pO_2-step changes between 0.2 and 0.4 atm. The apparent value of the surface exchange coefficient, k_{chem}, is found to vary with the loading amount and ionic conductivity of the coated phase whilst, as expected, the chemical diffusion coefficient D_{chem} remains invariant with the applied coating. Partial coverage of the LSCF surface with non-ionic conductive Gd_2O_3 or CeO_2 lowers the value of k_{chem} relative to that observed for bare LSCF, which is attributed to surface blocking effects. In contrast, partial coverage of LSCF with GCO electrolyte particles enhances the apparent value of k_{chem} up to a factor of ~6 compared to bare LSCF. The data of pulse isotope exchange (PIE) measurements show that the surface exchange reaction on bare LSCF is predominantly limited by dissociative adsorption of O_2. Different mechanisms for the improved oxygen surface exchange kinetics after partially covering the LSCF surface with GCO are discussed.

Introduction

The perovskite-structured oxide $La_{0.58}Sr_{0.4}Co_{0.2}Fe_{0.8}O_{3-\delta}$ (LSCF) is the state-of-the-art cathode material for the intermediate-temperature solid oxide fuel cell (IT-SOFC), owing to its high electrocatalytic activity for the oxygen reduction reaction (ORR), high electronic and ionic conductivities, and adequate compatibility with other cell components.[1–6] Since the cathode polarization contributes most to the energy losses in a SOFC, increasing at lower operating temperatures, to date significant research is still devoted to enhance the performance for the ORR.[5,7,8]

Possible oxygen reduction pathways for a mixed-conducting SOFC cathode material are schematically illustrated in Fig. 1. It is generally believed that bulk and surface pathways compete in determining the rate of incorporation of oxygen into the electrolyte.[5] The relative contribution of both pathways to the ORR kinetics is assumed to depend on the characteristic surface and bulk diffusion lengths, and the total length of the three-phase boundaries (TPBs). The porous microstructure of the cathode backbone structure (porosity, tortuosity, morphology, *etc.*) can be optimized to maximize the TPB area, and also the ionic, electronic and gas transport properties inside the electrode.[6,9]

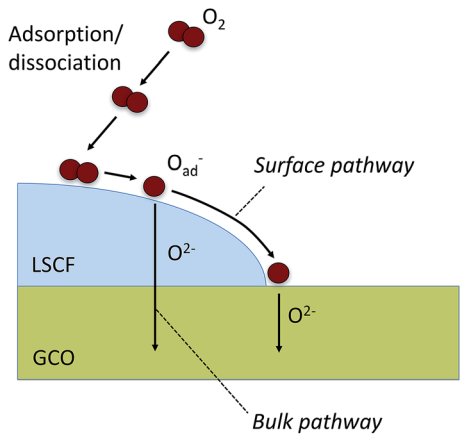

Fig. 1 Schematic illustration of bulk and surface pathways for a mixed-conducting SOFC cathode (exemplified for LSCF and GCO).

[a]Electrochemistry Research group, Membrane Science and Technology, MESA+ Institute for Nanotechnology, University of Twente, P.O. Box 217, Enschede, The Netherlands. E-mail: h.j.m.bouwmeester@utwente.nl; Fax: +31 53 4892336; Tel: +31 53 4892202

[b]CAS Key Laboratory of Materials for Energy Conversion, Department of Materials Science and Engineering, University of Science and Technology of China, Hefei, 230026, P. R. China

† Present address: U.S.-Pakistan Center for Advance Studies in Energy (USPCAS-E), University of Engineering and Technology, Peshawar, Khyber Pakhtunkhwa, Pakistan.

‡ Present address: Forschungszentrum Jülich GmbH Institute of Energy and Climate Research Materials Synthesis and Processing (IEK-1), 52425 Jülich, Germany.

Surface modification through infiltration of active components offers a complementary route to enhance the oxygen surface exchange kinetics of the mixed conductor and thus improving the ORR kinetics.[9–11] Significant enhancement of the oxygen surface exchange kinetics and/or cathode functionality has been found after coating LSCF with nanoparticles of solid oxide electrolytes such as $Sm_xCe_{1-x}O_{2-x/2}$ (SCO),[12–14] $Y_xCe_{1-x}O_{2-x/2}$ (YCO)[15] and $Gd_xCe_{1-x}O_{2-x/2}$ (GCO).[16,17] Similar enhancements have been reported for other mixed conductors, including $La_{0.6}Sr_{0.4}Co_{0.8}Fe_{0.2}O_{3-\delta}$,[18] $Sr_2Fe_{1.5}Mo_{0.5}O_{6-\delta}$,[19] $La_{0.85}Sr_{0.15}MnO_{3-\delta}$,[20] and $LaNi_{0.6}Fe_{0.4}O_{3-\delta}$ (ref. 21) after decorating their surfaces with nanoparticles of solid oxide electrolytes. The detailed mechanism behind the performance enhancements is, however, poorly understood. Hong *et al.*[13] attributed the improved surface exchange properties of LSCF after coating with SCO nanoparticles to a synergistic oxygen incorporation at the TPBs. To further investigate the role of ionic conductivity of the coating phase on surface exchange kinetics, we have measured the surface exchange properties of LSCF before and after coating with a porous nano-particulate layer of Gd_2O_3, CeO_2, or GCO. The former two materials are non-ionic conductive,[22] besides being precursors for the preparation of the solid oxide electrolyte GCO. Electrical conductivity relaxation (ECR) measurements are performed on uncoated and coated LSCF specimens, whilst ^{18}O–^{16}O pulse isotope exchange (PIE) measurements (on powders) are performed to gain more insight into the mechanism of oxygen exchange on pure LSCF.

Experimental

Sample preparation and characterisation

$La_{0.58}Sr_{0.4}Co_{0.2}Fe_{0.8}O_{3-\delta}$ (LSCF) powder was prepared *via* spray drying using an aqueous nitrate precursor solution containing appropriate amounts of the cations.[1] The obtained powder was calcined at 900 °C in air for 5 h, and subsequently ball-milled in ethanol for 10 h to achieve an average particle size (d_{50}) of ~300 nm. After drying the powder was uniaxially pressed at 30 MPa, followed by isostatic pressing at 400 MPa, into pellets. These were sintered at 1200 °C for 10 h in air, using heating and cooling rates of 5 °C min^{-1}, to a relative density of above 97% of the theoretical value as measured by Archimedes' method. Thin rectangular bars of size 12 mm × 6 mm × 0.5 mm were cut out of the sintered pellets, and the largest surfaces polished using a 1 μm grade alumina abrasive. The ceramic bars were ultrasonically cleaned in ethanol for 15 min prior to use for dip coating and ECR experiments.

Stable dip-coating suspensions of Gd_2O_3, CeO_2 and GCO ($Gd_{0.2}Ce_{0.8}O_{1.9}$) were obtained by mixing commercially available nanopowders (Sigma Aldrich Co.) with ethanol and polyvinyl butyral (PVB) binder, and subsequent ball milling for 24 h. The weight ratio of ethanol, oxide powder and PVB in the suspensions was 10 : 0.5 : 0.5. The dip-coated bars were dried for 6 h at 25 °C, and subsequently heat treated in two steps for firm adhesion of the coated particles on the LSCF surface, first at 600 °C for 4 h to remove the organic binder, and then at 1000 °C for 2 h, using heating and cooling rates of 5 °C min^{-1} in air. Repeating the dip-coating–heating procedure increased the deposition of the nano-particulate phase on the sample surface. The loading amount was measured with a high precision weighing balance.

The phase composition of powders used in this work was checked by X-ray powder diffraction (Bruker D2 PHASER, equipped with a LYNXEYE™ detector) using Cu-K_α radiation. Particle size distributions and BET surface areas of the powders were determined using the Mastersizer 2000 (Malvern Instruments) and Gemini VII 2390 (Micromeritics), respectively. Secondary electron (SE) and backscattered electron (BSE) scanning electron microscopy (SEM, JSM-6010LA) images were recorded to investigate the microstructure of the samples before and after the ECR experiments.

Electrical conductivity relaxation (ECR)

A four-probe dc technique was used to collect conductivity data. Gold wires 0.25 mm in diameter (Alfa Aesar, 99.999%) were attached to each bar end, while two additional gold wires were wrapped 0.2–0.4 cm from each bar end. Gold paste (MaTeck Co., Germany) was used to ensure good electrical contact, which was further used to completely cover both bar ends. The sample was then mounted on a holder and placed inside an alumina cell with an internal volume of about 2.6 cm^3 for measurements. The transient electrical conductivity was measured following oxidation and reduction step changes in pO_2 between 0.2 and 0.4 atm. Measurements were conducted during heating and cooling in the temperature range 700–900 °C. The temperature was changed stepwise with intervals of 50 °C, using heating and cooling rates of 5 °C min^{-1}, and with a dwell time at each temperature of 30 min before data acquisition. Three subsequent oxidation and reduction step changes were performed at each temperature, which lasted in total for approximately 30–60 min. The total time to complete a series of measurements on a given sample took about 15 h. The pO_2 of the gas streams was adjusted by mixing nitrogen and oxygen, and monitored by an oxygen sensor (Systech Model Zr893/4). Two gas flow pathways with different pO_2 values were maintained in the system, one of which was fed through the cell. A computer-controlled 4-way valve was utilized to rapidly switch between both pathways to achieve an instantaneous step change in pO_2. The gas flow through the cell and current through the sample were fixed at 300 ml min^{-1} and 500 mA, respectively. The flushing time constant calculated assuming idealised continuous-flow stirred tank reactor (CSTR) conditions was typically less than 0.1 s.

The transient conductivity after each pO_2 step change was normalised according to eqn (1) and fitted to eqn (2)–(4) to obtain the chemical diffusion coefficient D_{chem}, and the surface exchange coefficient k_{chem}.

$$g(t) = \frac{\sigma(t) - \sigma_0}{\sigma_\infty - \sigma_0} \tag{1}$$

$$g(t) = 1 - \prod_{i=x,y} \sum_{m=1}^{\infty} \frac{2{L_i}^2}{{\beta_{m,i}}^2\left({\beta_{m,i}}^2 + {L_i}^2 + L_i\right)} \frac{\tau_{m,i}}{\tau_{m,i} - \tau_f} \left(\exp\left(-\frac{t}{\tau_{m,i}} \right) - \frac{\tau_f}{\tau_{m,i}} \exp\left(-\frac{t}{\tau_f} \right) \right) \tag{2}$$

$$\tau_{m,i} = \frac{{b_i}^2}{D_{\text{chem}}{\beta_{m,i}}^2} \quad (3)$$

$$L_i = \frac{b_i}{L_c} = \beta_{m,i} \tan \beta_{m,i} \quad (4)$$

In these equations, $g(t)$ is the normalized conductivity, σ_0 and σ_∞ are the conductivities at time $t = 0$ and $t = \infty$, respectively, τ_f the flushing time constant of the reactor, and $2b_i$ the sample dimension along coordinate i, whilst $\beta_{m,i}$ are the non-zero roots of eqn (3). $L_c = D_{\text{chem}}/k_{\text{chem}}$ is the critical length scale below which oxygen surface exchange becomes predominant over bulk oxygen diffusion in determining the rate of re-equilibration after the pO_2 step change. Values of D_{chem}, and likewise of k_{chem}, calculated from oxidation runs at each temperature were averaged. Similarly, this was done for data obtained from reduction runs. Detailed descriptions of the ECR technique and the model used for data fitting are given elsewhere.[23,24]

Pulse isotopic exchange (PIE)

Sintered pellets of LSCF were crushed into a coarse powder, and then sieved through a 125 μm mesh. The obtained powder was annealed in air at 950 °C for 10 h, and sieved again for removal of formed aggregates. The LSCF powder was loaded in the centre of a quartz tubular micro-reactor with an inner diameter of 2 mm. Quartz wool plugs were used to secure the packed powder bed. The length and mass of the packed bed were 13 mm and 160 mg, respectively. $^{16}O_2$ mixed with Ar was used as the carrier gas, and fed through the reactor with a total flow rate of 50 ml min^{-1} (NTP). Gases were dried using Chrompack gas clean moisture filters before entering the reactor. The oxygen isotope gas was purchased from Cambridge Isotope Laboratories, Inc. (>97 atom% $^{18}O_2$).

A six-port valve with a 500 μl sample loop was used for injection of the $^{18}O_2/N_2$ pulse into the $^{16}O_2$/Ar carrier gas, the pulse having the same pO_2 as the carrier gas. The diluent nitrogen in the pulse was used for internal calibration of the mass spectrometer (Omni Star TM GSD 301 Pfeiffer-Vacuum). The mean residence time of the reactor varied between 10 and 30 ms, depending on the temperature. Prior to exchange measurements, the packed bed was pre-treated at 850 °C for 0.5 h in synthetic air to remove possibly adsorbed water and CO_2, and subsequently cooled down to 50 °C at a rate of 5 °C min^{-1}.

PIE measurements were performed in the temperature range of 50–575 °C and at a pO_2 of 0.21 atm. Averaged values of the $^{18}O_2$ and $^{16}O^{18}O$ effluent fractions in three pulse experiments, at a given temperature, were used for calculation of the exchange rate. The reactor was equilibrated for 0.5 h at each temperature before data acquisition. The overall surface exchange rate, $\Re_0$ [mol (O) m^{-2} s^{-1}], was calculated from[25]

$$\Re_0 = \frac{2F_m}{S} \ln\left(\frac{f_i^{18}}{f_e^{18}}\right) \quad (5)$$

where f_i^{18} and f_e^{18} are the ^{18}O isotope fractions in the pulse at the inlet and exit of the reactor, respectively, F_m is the O_2 molar flow rate through the packed bed, S the total surface area of the oxide powder. The fraction f^{18} is calculated from $f^{18} = 0.5f^{34} + f^{36}$. The exchange rate $\Re_0$ can be broken down into the rates of successive steps. Assuming a two-step consecutive mechanism for the exchange reaction,

$$O_2 + 2(\,)_{ad} \overset{\Re_{ads}}{\rightleftharpoons} 2O_{ad}$$
$$O_{ad} + (\,)_s \overset{\Re_{inc}}{\rightleftharpoons} O_s + (\,)_{ad} \quad (6)$$

where O_{ad} is the adsorbed oxygen, O_s the incorporated oxygen, $(\,)_{ad}$ the adsorption site, and $(\,)_s$ the lattice oxygen vacancy. It follows,[26]

$$\Re_0 = \frac{\Re_{ads}\Re_{inc}}{\Re_{ads} + \Re_{inc}} = p\Re_{ads} \quad (7)$$

where $\Re_{ads}$ and $\Re_{inc}$ are the rates of oxygen dissociative adsorption and incorporation, respectively. The quantity p represents the probability of each atom in the O_2 molecule for being incorporated into the oxide bulk and is calculated from

$$f_e^{36} = \left(\frac{(1-p)}{1-2p} f_i^{18}\right)^2 \exp\left(-\frac{2\Re_0 S}{F_m}\right) + \left(f_i^{36} - \left(\frac{(1-p)}{(1-2p)^{1/2}} f_i^{18}\right)^2\right) \exp\left(\frac{\Re_0 S}{F_m}\right) \quad (8)$$

where f_i^{36} and f_e^{36} are the $^{36}O_2$ fractions in the pulse at the inlet and exit of the reactor, respectively. More details of the PIE technique and theory are given elsewhere.[27,28]

Results and discussion

Electrical conductivity relaxation

SEM micrographs of bare and coated LSCF bars used in the ECR experiments are shown in Fig. 2. In these figures the coating oxide has a higher brightness than the bare surface. Fig. 2b–d show that the GCO nanoparticles are uniformly distributed over the LSCF surface, producing a highly porous coating layer. The particle size (~300 nm) is notably smaller than the grain size of ~10 μm of the underlying LSCF substrate (Fig. 2a). The heat treatment at 1000 °C induces significant agglomeration of the Gd_2O_3 and CeO_2 nanoparticles, resulting in non-uniform coating layers, as seen from Fig. 2e–f. In both cases, distinct regions of bare LSCF remain visible even after repeated dip-coating. No attempt was made to optimize the heat treatment procedure in order to obtain more homogenous coating layers, although it is anticipated that the presence of inhomogeneities will affect the apparent surface exchange rate. XRD showed no evidence of second or impurity phases in the oxide powders obtained in this study.

Normalized conductivity curves acquired for bare and coated LSCF bars at 800 °C, following pO_2 step changes from 0.20 to 0.40 atm are shown in Fig. 3. Compared to bare LSCF, the time needed for re-equilibration depends on the nature and amount of the coated nano-particulate oxide. The solid lines are the best fit of experimental data to eqn (2)–(4), revealing that under the

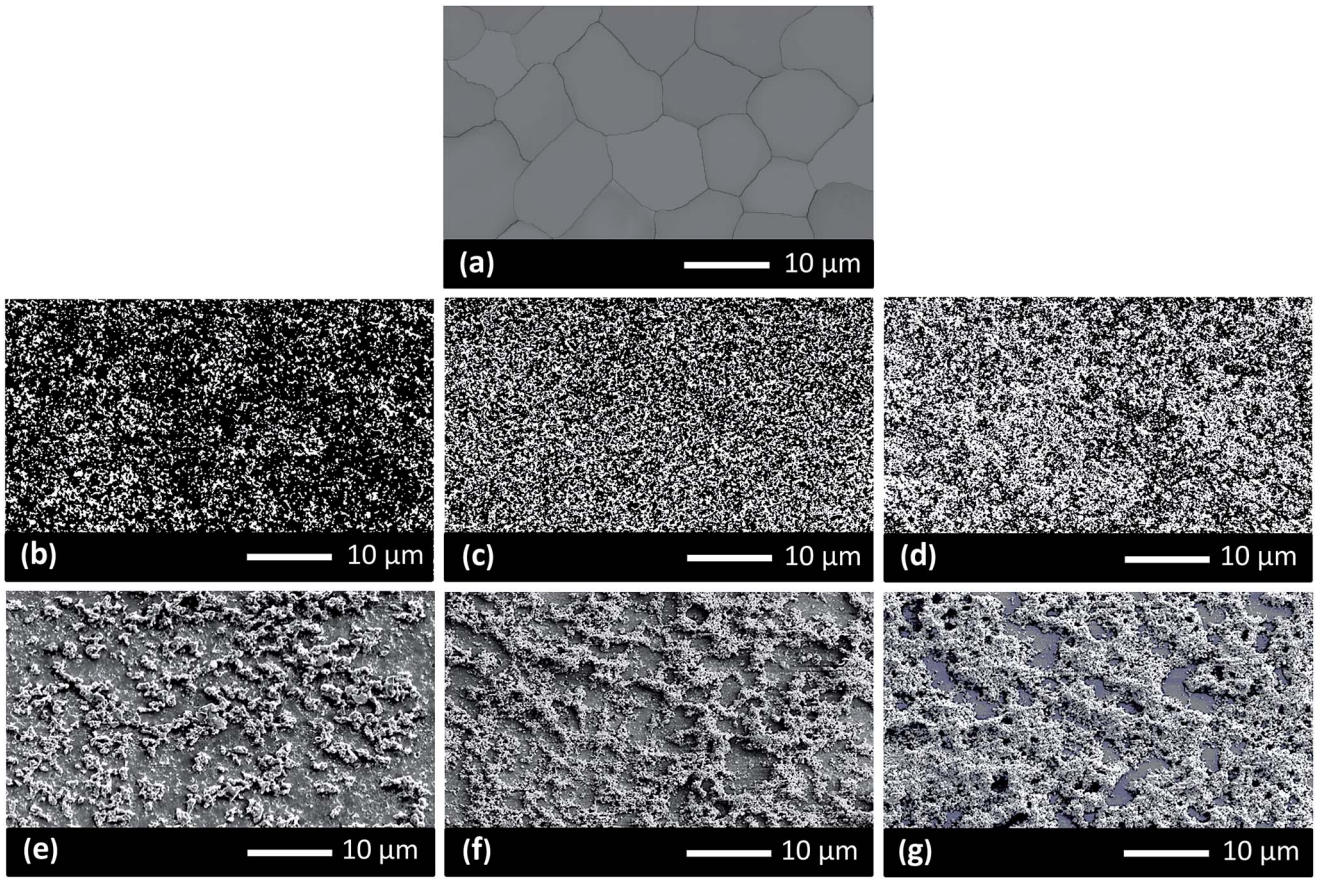

Fig. 2 Secondary electron SEM image of (a) LSCF surface, and backscattered electron SEM images of LSCF coated with (b) 0.21 mg cm^{-2} GCO, (c) 0.35 mg cm^{-2} GCO, (d) 0.56 mg cm^{-2} GCO, (e) 0.50 mg cm^{-2} Gd_2O_3, (f) 0.79 mg cm^{-2} CeO_2, and (g) 1.16 mg cm^{-2} CeO_2.

applied experimental conditions the relaxation behaviour for all samples is under a mixed control of diffusion and surface exchange. The critical length scale, L_c, is found to be in the range $30 < L_c < 300$ μm. The values of D_{chem}, and similarly for k_{chem}, obtained from the data of measurements during heating and cooling were virtually the same. These observations suggest that neither LSCF nor the applied coating degraded within the time scale of the experiments. SEM examinations showed the same distribution and morphology of the coating layers as before the ECR experiments.

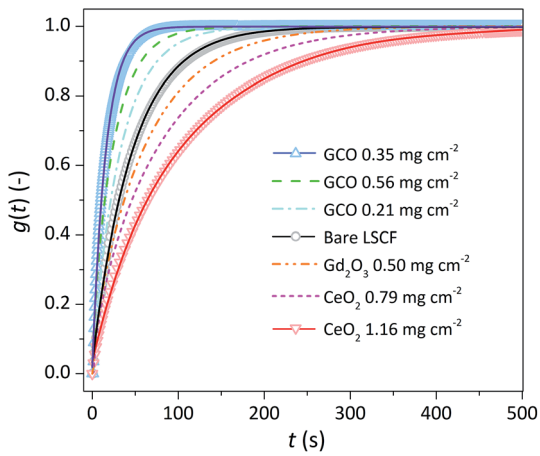

Fig. 3 Normalized conductivity relaxation curves for bare LSCF and samples coated with Gd_2O_3, CeO_2 or GCO. Data acquired at 800 °C after pO_2 step changes from 0.20 to 0.40 atm (oxidation runs). The solid lines represent the least squares fits to eqn (1)–(3).

Fig. 4a shows that values of D_{chem} for each of the samples obtained from fitting agree within the experimental error. The average activation energy is 128 ± 5 kJ mol^{-1}. Fig. 4b further shows that D_{chem} extracted from the data of oxidation and reduction runs agree well, indicating that the applied pO_2 step size is small enough to assume a constant value of D_{chem} during re-equilibration. As seen from Fig. 4b, a good agreement is found with literature values of D_{chem} acquired under conditions of pO_2 and temperature similar to those in the present study.[29,30] The present observations confirm our general expectation that the oxygen diffusivity in LSCF is not affected by surface coating.

Fig. 5 shows the Arrhenius plots of the apparent values of k_{chem} for each of the samples. Activation energies calculated from these data are listed in Table 1. There is a slight but significant trend in the activation energy, which varies with the nature and amount of the applied coating. The results in Fig. 5 show that the values of k_{chem} of LSCF are significantly affected by the surface treatment. This is further visualized in Fig. 6, which displays the trend in k_{chem}, at different temperatures,

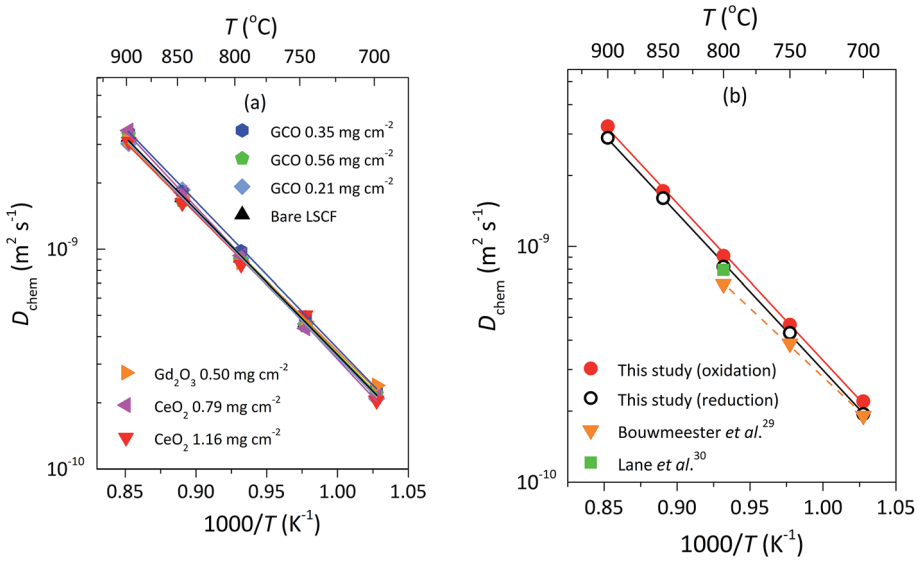

Fig. 4 Arrhenius plot of D_{chem} for (a) bare LSCF and coated samples (oxidation runs), and (b) bare LSCF, showing the close agreement between values extracted from conductivity transients recorded after oxidation and reduction step changes between $pO_2 = 0.20$ and 0.40 atm. Published data of D_{chem} are shown for comparison.

with coating oxide and the applied amount of coating. At all temperatures covered by the experiments, k_{chem} is found to decrease upon coating with non-ionic conductive Gd_2O_3 or CeO_2, *i.e.*, up to a factor of ~5 after coating with 1.16 mg cm^{-2} CeO_2 compared to bare LSCF. This observation is tentatively explained by the associated blocking of sites involved in the oxygen exchange reaction. In contrast, coating with 0.35 mg cm^{-2} of GCO causes an increase of k_{chem} by a factor of ~6 compared to bare LSCF. As seen from Fig. 6, further increasing the surface coverage of GCO adversely affects the rate of oxygen exchange. The results obtained from ECR experiments are further discussed below.

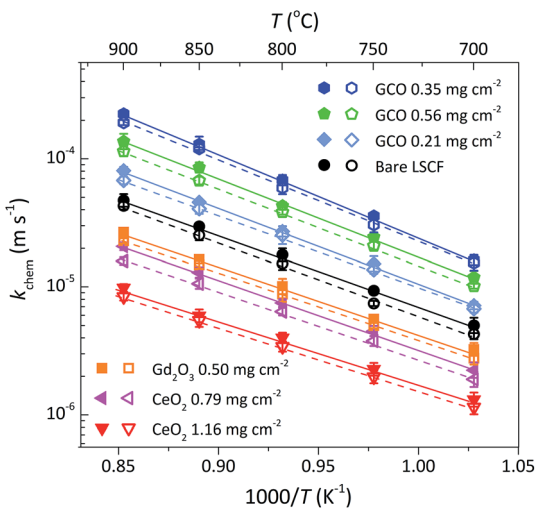

Fig. 5 Arrhenius plot of k_{chem} for bare LSCF and coated samples. Data extracted from conductivity transients recorded after oxidation (full symbols) and reduction (empty symbols) step changes between $pO_2 = 0.20$ and 0.40 atm.

Pulse isotopic exchange

To gain insight into the mechanism of surface exchange on bare LSCF, PIE measurements were conducted. Fig. 7a shows the temperature dependence of the oxygen isotope fractions measured, at $pO_2 = 0.21$ atm, at the exit of the reactor loaded with the LSCF powder after pulsing $^{18}O_2$ through the reactor. At a temperature of around 500 °C, slightly more than half of the original fraction of $^{18}O_2$ in the pulse volume is converted into $^{16}O_2$ and $^{16}O^{18}O$. The typical signature of a maximum in the temperature dependence of the $^{16}O^{18}O$ fraction indicates that, in accord with the two-step model eqn (6) for the oxygen exchange reaction, the rate of dissociative adsorption ($\Re_{ads}$) and that of the subsequent incorporation of oxygen adatoms into the bulk ($\Re_{inc}$) compete with each other in determining the overall surface exchange rate ($\Re_0$). Fig. 7b shows the Arrhenius plot of $\Re_0$, $\Re_{ads}$, and $\Re_{inc}$ calculated from these data, using eqn (7) and (8). From these results it emerges that the oxygen surface

Table 1 Apparent activation energies of k_{chem} from the data of ECR experiments on bare LSCF and samples coated with GCO, Gd_2O_3 or CeO_2. Standard errors are given in parentheses and refer to the least significant decimals

Material	Loading content (mg cm^{-2})	Activation energy (kJ mol^{-1}) Oxidation run	Reduction run
GCO	0.35	123 (5)	120 (7)
GCO	0.56	115 (4)	115 (6)
GCO	0.21	113 (5)	108 (6)
LSCF	0	109 (3)	111 (5)
Gd_2O_3	0.5	103 (6)	101 (3)
CeO_2	0.79	104 (2)	101 (4)
CeO_2	1.16	95 (3)	95 (2)

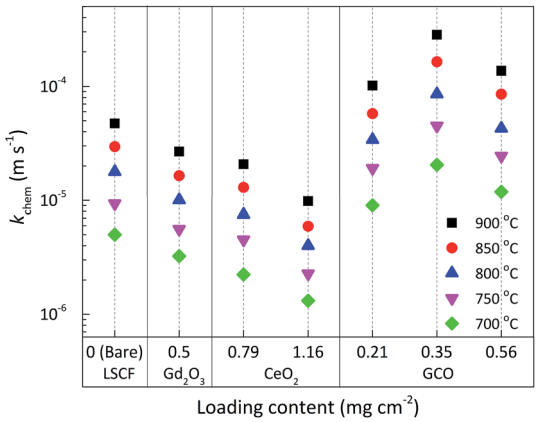

Fig. 6 Variation in k_{chem} at different temperatures with the amount (mg cm^{-2}) of Gd_2O_3, CeO_2 or GCO coated on LSCF. The first column shows the corresponding value for bare (uncoated) LSCF. For clarity reasons only data obtained from oxidation runs are shown.

exchange rate on pure LSCF is predominantly limited by $\Re_{ads}$, as has been observed for related perovskite mixed conductors.[27] Activation energies of the different exchange rates are listed in Table 2.

Fig. 8 compares the temperature dependence of the surface exchange coefficient k_s from PIE and ECR experiments. Calculations were performed using the relationships

$$k_{chem} = k_s W \quad (9)$$

and

$$\Re_0 = k_s c_O \quad (10)$$

Table 2 Apparent activation energies (kJ mol^{-1}) of the rates of overall oxygen surface exchange ($\Re_0$), oxygen dissociative adsorption ($\Re_{ads}$), and oxygen incorporation ($\Re_{inc}$) for LSCF. Standard errors are given in parentheses and refer to the least significant decimals

Material	$\Re_0$	$\Re_{ads}$	$\Re_{inc}$
LSCF	131 (3)	132 (3)	119 (6)

where $W = 0.5\partial \ln pO_2/\partial \ln c_O$ is the thermodynamic factor, and c_O is the oxygen concentration in LSCF. The thermodynamic factor W was calculated using published data of the oxygen nonstoichiometry of A-site stoichiometric $La_{0.6}Sr_{0.4}Co_{0.2}Fe_{0.8}O_{3-\delta}$ as a function of pO_2 determined by thermogravimetry.[31] The average activation energies of k_s calculated from the data of both experiments, 157 ± 5 and 161 ± 7 kJ mol^{-1}, respectively, agree within the experimental error. Note further from Fig. 8 the excellent agreement between the extrapolated values of k_s from both experiments, which provides evidence in support of the validity of eqn (9) for LSCF.

Mechanism of oxygen exchange on GCO-coated LSCF

The results from ECR experiments show that coating the LSCF surface with GCO promotes oxygen exchange. Ionic conductivity of the additive oxide is seemingly essential since a decrease in k_{chem} is found when the LSCF surface is partially covered with non-ionic conductive Gd_2O_3 or CeO_2 (see Fig. 5 and 6). The observations are consistent with those previously made by Hong *et al.*,[13] showing that the exchange rate of LSCF coated with $Sm_xCe_{1-x}O_{2-x/2}$ (SCO) in the range $0.05 \leq x \leq 0.40$ increases with the ionic conductivity of the electrolyte phase. Sirman and Kilner[32] demonstrated that the surface exchange coefficient k_s of

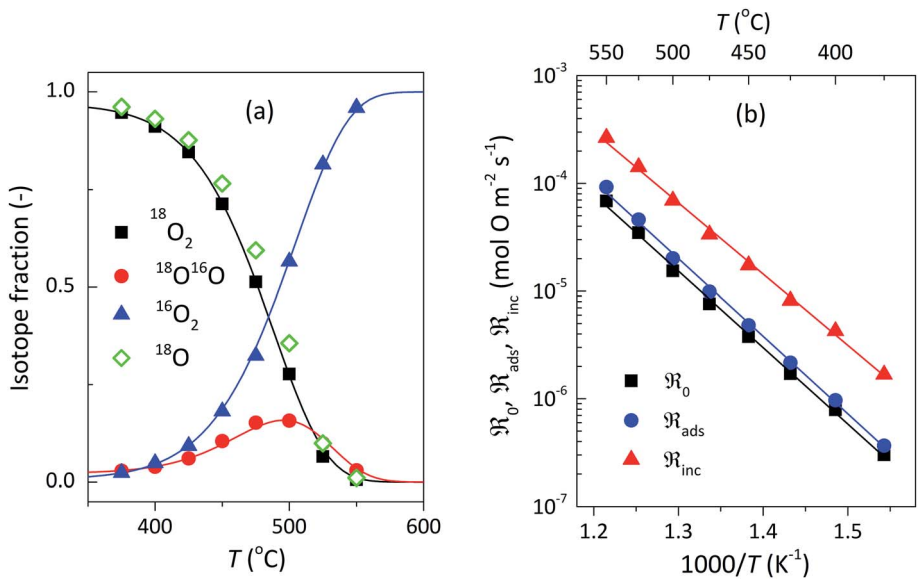

Fig. 7 (a) Oxygen isotope fractions f^{18}, f^{36}, f^{34} and f^{32} (for ^{18}O, $^{18}O_2$, $^{18}O^{16}O$, and $^{16}O_2$, respectively) as a function of temperature from PIE measurements on the LSCF powder, at $pO_2 = 0.21$ atm, and (b) Arrhenius plots of the exchange rates $\Re_0$, $\Re_{ads}$ and $\Re_{inc}$. The drawn lines in (a) have been calculated on the basis of the two-step model eqn (5) for the oxygen exchange reaction. Constant activation energies for $\Re_{ads}$ and $\Re_{inc}$ are assumed over the range of temperature covered by the experiments.

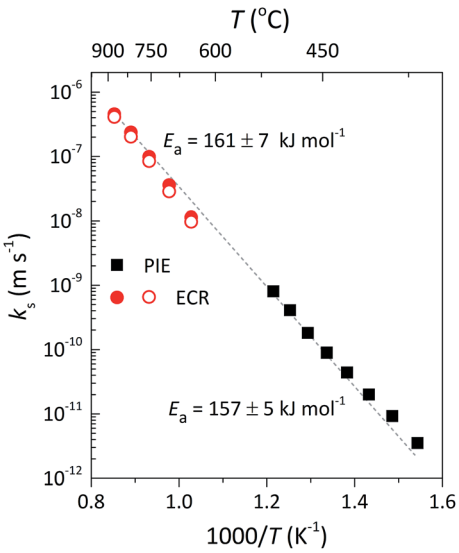

Fig. 8 Comparison of the surface exchange coefficient k_s obtained from PIE and ECR experiments. Filled and open circles represent data obtained from oxidation and reduction step changes during ECR experiments, respectively. The dashed line serves as a guide to the eye.

GCO can be increased by two orders of magnitude by decorating with LSCF particles. This was explained by the authors in terms of LSCF becoming the active site for exchange and/or electrons becoming available at the TPB regions. The observed oxygen exchange enhancement for LSCF upon addition of GCO particles in this study in a way comes to some surprise since at the temperatures and oxygen partial pressures covered by the experiments the reported exchange rate of pure LSCF is orders of magnitude higher than that of GCO.[30,32,33]

A spillover type of mechanism[34] may be assumed to account for the observed oxygen exchange enhancement upon addition of GCO particles to the LSCF surface. It is envisaged, as is schematically shown in Fig. 9, that dissociative adsorption of O_2 occurs on the LSCF surface, followed by diffusion of activated oxygen species across the surface towards the additive GCO, where the incorporation of the oxygen anions at the TPB is considered to be more facile. The latter may be reconciled, at least partly, by the higher oxygen nonstoichiometry of GCO ($\delta \approx 0.1$) relative to that of LSCF ($0.002 \leq \delta \leq 0.040$)[31] in the experimental range of temperatures 700–900 °C. Hence, in this view the

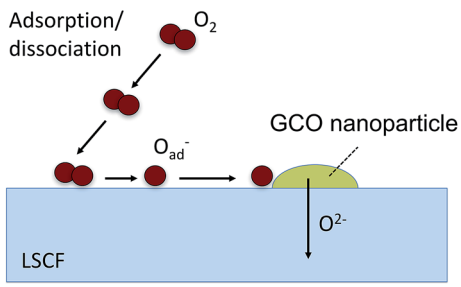

Fig. 9 Spillover type of mechanism for oxygen exchange after coating LSCF with GCO nanoparticles.

GCO particles act as portals for the transfer of oxygen anions to the (underlying) LSCF substrate. Hong *et al.*[13] were the first to attribute the enhancement in the surface exchange rate of LSCF after coating with electrolyte particles to fast oxygen incorporation at the TPBs. A similar spillover of adsorbates across the TPBs was proposed to account for the enhanced exchange rate exhibited by composites $La_{0.6}Sr_{0.4}Co_{0.2}Fe_{0.8}O_{3-\delta}$–$Gd_{0.1}Ce_{0.9}O_{1.95}$ (LSCF–GCO),[35] $La_{0.6}Sr_{0.4}Co_{0.2}Fe_{0.8}O_{3-\delta}$–$Sm_{0.2}Ce_{0.8}O_{1.9}$ (LSCF–SCO),[36–38] $La_{0.8}Sr_{0.2}MnO_{3-\delta}$–$Y_{0.16}Zr_{0.84}O_2$ (LSM–YSZ),[39] and $Sr_2Fe_{1.5}Mo_{0.5}O_{6-\delta}$–$Sm_{0.2}Ce_{0.8}O_{1.9}$ (SFM–SCO).[40]

The above-cited spillover mechanism may be conjectured if dissociation of O_2 on the LSCF surface is relatively fast compared to incorporation of the formed oxygen adatoms, while the latter is believed to proceed much faster *via* the surface of the additive GCO. DFT calculations for LSCF performed by Kuklja *et al.*[41] indeed support dissociative adsorption of O_2 (forming two oxygen O_{ad}^- ions) to be energetically more favourable than molecular adsorption (forming an adsorbed superoxide $O_{2,ad}^-$ ion). The calculations, however, predict a high-energy barrier for O_{ad}^- migration of ~2 eV, which clearly is not in favour of a spillover mechanism. A much lower energy barrier (~0.8–0.9 eV) is predicted for surface oxygen vacancy migration, which prompted the authors to propose an oxygen exchange mechanism for single-phase LSCF in which 'on-site' oxygen incorporation is facilitated by migration of oxygen vacancies towards the adsorbed O_{ad}^- ions.

Another argument to exclude a spillover mechanism comes from the results of PIE experiments in this work (Fig. 7), revealing that the exchange rate on bare LSCF is predominantly limited by the rate of dissociative adsorption ($\Re_{ads}$). Assuming oxygen incorporation *via* the additive GCO electrolyte to proceed infinitely fast, the maximum enhancement can be estimated *via* eqn (7), letting $\Re_{inc} \gg \Re_{ads}$. With neglect of effects related to surface coverage, the calculations show a maximum enhancement of a factor of 1.2–1.3, which is much less than the experimentally observed value of ~6. Along the same line of thought, the data in Fig. 7b indicate that dispersion of agents on the LSCF surface enhancing the rate of $\Re_{ads}$ rather than $\Re_{inc}$ is a much more promising strategy to promote the exchange rate for LSCF.

Druce *et al.*[35] proposed a scavenging of blocking impurities such as silica and calcia to account for the enhanced exchange rate of GCO in LSCF–GCO composites. Develos-Bagarinao *et al.*[42] showed evidence for an enhanced exchange rate of nano-structured GCO. For these reasons, a direct contribution of GCO nanoparticles to the apparent overall exchange rate of the coated samples cannot be excluded. In the present study, the availability of electrons through emission or tunnelling from LSCF to GCO may also enhance the exchange rate of GCO. Alternatively, GCO may actively contribute to the adsorption of molecular oxygen from the gas phase. Rather than the diffusion of dissociated oxygen across the LSCF surface to the phase boundary with the additive oxide (Fig. 9), a spillover of oxygen intermediates from the GCO surface towards the LSCF surface may be conceived. It is clear that further scientific studies are warranted to explain the present observations and/or to validate the alternative proposed mechanisms. Finally,

following previous investigations of oxygen exchange at mesh-type $La_{0.85}Sr_{0.15}MnO_3$, Au and Pt electrodes on yttria-stabilized zirconia,[43–45] the authors would like to advocate the use of micro-patterned, dense GCO structures on LSCF in conjunction with ^{18}O–^{16}O isotope exchange with subsequent imaging secondary ion mass spectroscopy (SIMS) analysis as a possible tool to visualize and quantify the preferred exchange pathway.

Conclusions

Data of ECR measurements have been presented on dense LSCF ceramics either bare or coated with a porous nano-particulate layer of Gd_2O_3, CeO_2, or GCO in the temperature range 700–900 °C. The apparent value of the surface exchange coefficient, k_{chem}, is found to vary with loading amount and ionic conductivity of the coated phase, whilst, as expected, the chemical diffusion coefficient D_{chem} remains invariant for the different samples. The partial coverage of the LSCF surface with non-ionic conductive Gd_2O_3 or CeO_2 decreases the value of k_{chem}, which is attributed to surface blocking effects. In contrast, the partial coverage with particles of the oxide electrolyte GCO increases k_{chem} up to a factor of ~6 compared to pure LSCF. The latter observation is consistent with the results of previous studies, showing that the decoration of solid electrolyte particles on the surface of a mixed-conducting cathode represents an attractive approach for improving the ORR kinetics (for references, see the Introduction). The results of PIE measurements demonstrate that surface exchange on bare LSCF is predominantly limited by dissociative adsorption of O_2. In conjunction with the data from DFT analysis,[41] the results are evaluated as evidence to exclude a spillover mechanism, involving fast migration of activated oxygen across the LSCF surface towards GCO, followed by incorporation of oxygen anions at the TPB. Alternative mechanisms for the improved oxygen surface exchange kinetics observed for LSCF by partial covering with GCO are briefly discussed.

Acknowledgements

S. Saher gratefully acknowledges financial support from the Education, Audiovisual and Cultural Executive Agency (EACEA) under the program European Doctorate in Membrane Engineering (EUDIME, FPA 2011-0014).

References

1 F. Tietz, V. A. C. Haanappel, A. Mai, J. Mertens and D. Stöver, *J. Power Sources*, 2006, **156**, 20–22.
2 A. Mai, V. Haanappel, S. Uhlenbruck, F. Tietz and D. Stöver, *Solid State Ionics*, 2005, **176**, 1341–1350.
3 H. J. Hwang, M. B. Ji-Woong, L. A. Seunghun and E. A. Lee, *J. Power Sources*, 2005, **145**, 243–248.
4 W. G. Wang and M. Mogensen, *Solid State Ionics*, 2005, **176**, 457–462.
5 S. Adler, *Chem. Rev.*, 2004, **104**, 4791–4843.
6 C. Sun, R. Hui and J. Roller, *J. Solid State Electrochem.*, 2010, **14**, 1125–1144.
7 N. Mahato, A. Banerjee, A. Gupta, S. Omar and K. Balani, *Prog. Mater. Sci.*, 2015, **72**, 141–337.
8 Z. Gao, L. V. Mogni, E. C. Miller, J. G. Railsback and S. A. Barnett, *Energy Environ. Sci.*, 2016, **9**, 1602–1644.
9 J. M. Vohs and R. J. Gorte, *Adv. Mater.*, 2009, **21**, 943–956.
10 Z. Jiang, C. Xia and F. Chen, *Electrochim. Acta*, 2010, **55**, 3595–3605.
11 D. Ding, X. Li, S. Y. Lai, K. Gerdes and M. Liu, *Energy Environ. Sci.*, 2014, **7**, 552–575.
12 L. Nie, M. Liu, Y. Zhang and M. Liu, *J. Power Sources*, 2010, **195**, 4704–4708.
13 T. Hong, L. Zhang, F. Chen and C. Xia, *J. Power Sources*, 2012, **218**, 254–260.
14 F. Shen and K. Lu, *J. Power Sources*, 2015, **296**, 318–326.
15 T. Z. Sholklapper, H. Kurokawa, C. P. Jacobson, S. J. Visco and L. C. De Jonghe, *Nano Lett.*, 2007, **7**, 2136–2141.
16 H. J. Hwang, J.-W. Moon, S. Lee and E. A. Lee, *J. Power Sources*, 2005, **145**, 243–248.
17 M. Shah, P. W. Voorhees and S. A. Barnett, *Solid State Ionics*, 2011, **187**, 64–67.
18 T. E. Burye and J. D. Nicholas, *J. Power Sources*, 2015, **300**, 402–412.
19 L. Zhang, Y. Liu, Y. Zhang, G. Xiao, F. Chen and C. Xia, *Electrochem. Commun.*, 2011, **13**, 711–713.
20 X. Xu, Z. Jiang, X. Fan and C. Xia, *Solid State Ionics*, 2006, **177**, 2113–2117.
21 R. A. Budiman, T. Miyazaki, S. Hashimoto, K. Yashiro and T. Kawada, *Solid State Ionics*, 2016, **286**, 19–23.
22 H. Inaba and H. Tagawa, *Solid State Ionics*, 1996, **83**, 1–16.
23 J. E. ten Elshof, M. H. R. Lankhorst and H. J. M. Bouwmeester, *J. Electrochem. Soc.*, 1997, 1060–1067.
24 M. W. den Otter, H. J. M. Bouwmeester, B. A. Boukamp and H. Verweij, *J. Electrochem. Soc.*, 2001, **148**, J1–J6.
25 C.-Y. Yoo, B. A. Boukamp and H. J. M. Bouwmeester, *J. Solid State Electrochem.*, 2010, **15**, 231–236.
26 M. W. den Otter, B. A. Boukamp and H. J. M. Bouwmeester, *Solid State Ionics*, 2001, **139**, 89–94.
27 H. J. M. Bouwmeester, C. Song, J. Zhu, J. Yi, M. van Sint Annaland and B. A. Boukamp, *Phys. Chem. Chem. Phys.*, 2009, **11**, 9640–9643.
28 C.-Y. Yoo, B. A. Boukamp and H. J. M. Bouwmeester, *Solid State Ionics*, 2013, **262**, 668–671.
29 H. J. M. Bouwmeester, M. W. den Otter and B. A. Boukamp, *J. Solid State Electrochem.*, 2004, **8**, 599–605.
30 J. A. Lane, S. J. Benson, D. Waller and J. A. Kilner, *Solid State Ionics*, 1999, **121**, 201–208.
31 S. R. Bishop, K. L. Duncan and E. D. Wachsman, *J. Electrochem. Soc.*, 2009, **156**, B1242–B1248.
32 J. D. Sirman and J. A. Kilner, *J. Electrochem. Soc.*, 1996, **143**, L229–L231.
33 J. A. Lane and J. A. Kilner, *Solid State Ionics*, 2000, **136**, 927–932.
34 W. C. Conner and J. L. Falconer, *Chem. Rev.*, 1995, **95**, 759–788.
35 J. Druce, H. Téllez, T. Ishihara and J. A. Kilner, *Faraday Discuss.*, 2015, **182**, 271–288.

36 B. Hu, Y. Wang and C. Xia, *J. Power Sources*, 2014, **269**, 180–188.
37 B. Hu, Y. Wang and C. Xia, *J. Electrochem. Soc.*, 2015, **162**, F33–F39.
38 B. Hu, K. Guo, M. Li, Y. Li and C. Xia, *J. Electrochem. Soc.*, 2016, **163**, F190–F195.
39 Y. Ji, J. A. Kilner and M. F. Carolan, *Solid State Ionics*, 2005, **176**, 937–943.
40 Y. Wang, B. Hu, Z. Zhu, H. J. M. Bouwmeester and C. Xia, *J. Mater. Chem. A*, 2014, **2**, 136–143.
41 M. M. Kuklja, E. A. Kotomin, R. Merkle, Y. A. Mastrikov and J. Maier, *Phys. Chem. Chem. Phys.*, 2013, **15**, 5443–5471.
42 K. Develos-Bagarinao, H. Kishimoto, K. Yamaji, T. Horita and H. Yokokawa, *Nanotechnology*, 2015, **26**, 215401.
43 H. Kishimoto, N. Sakai, K. Yamaji, T. Horita, M. E. Brito, H. Yokokawa, K. Amezawa and Y. Uchimoto, 2008, **179**, 347–354.
44 T. Horita, K. Yamaji, N. Sakai, Y. Xiong, T. Kato, H. Yokokawa and T. Kawada, *J. Power Sources*, 2002, **106**, 224–230.
45 T. Horita, K. Yamaji, N. Sakai, H. Yokokawa, T. Kawada and T. Kato, *Solid State Ionics*, 2000, **127**, 55–65.